

Design of an Infrared LED for use in Medical Applications

R. Grady

I. MOTIVATION AND BACKGROUND

Of all the interesting features of LED lighting, the ability to create light of a specific wavelength has led to the application of LEDs in myriad scenarios. Some novel uses include optogenetics, agriculture, and disinfection. The use of LEDs in the medical field is of particular interest, due to their ability to help save lives and reduce patient discomfort. The use of UV light for disinfection in clinical settings is well documented. Another unique application, and the one we are interested in, is light-assisted medical procedures. By taking advantage of what is known as the Near Infrared (NIR) window in biological tissues, medical professionals can use NIR to see inside of a patient's tissues and vasculature [1]. Similar to the way in which the X-ray imaging system has allowed the health care sector to see our bones and the use of magnetic resonance imaging (MIR) has given us unprecedented access to the behavior of our brains and tissues, the use of NIR can help medical professionals perform their jobs in unique ways.

The use of NIR in medicine focuses entirely on non-invasive procedures. This range of wavelengths is unique in that the tissues and bones pass them through almost entirely, while hemoglobin in the blood is a strong absorber of NIR. Even more striking, the absorption rate for oxygenated hemoglobin (HbO_2) and deoxygenated hemoglobin (Hb) differ [2]. This gives the blood a different appearance under NIR investigation based on the oxygen content. The use of these properties can range from increasing the visibility of veins for use in delivering intravenous (IV) medications or taking blood samples, to NIR spectroscopy.

In particular, the use of NIR to image the vascular system for medicine delivery is a growing area. Technology to see a patient's veins has been largely based on the use of NIR imaging combined with computer processing. These technologies use NIR LEDs and cameras using IR filters to capture the images, after which the image is processed and projected back on to the patient's skin to give the appearance of a "see-through" window [3]. Some existing products include the VeinViewer, Vasculuminator, and AccuVein [4]. The projected imagery can be seen in Figure (1). These products promise to eliminate the need to insert a needle multiple times trying to find a vein. This is useful for patient comfort, as well as for medical assistance in environments such as battlefields and emergency sites increasing survival chances.



Figure 1: Commercial VeinViewer [5]

A major drawback to these technologies lies in the computer processing. Typically, the device would be attached to a computer allowing the processing to happen independent of the actual projector, but this limits the locations in which the devices may be utilized. Some handheld models, such as the VeinViewer Flex, are portable [5]. They rely on lithium ion batteries or external power sources and are able to operate for up to 4 hours on a single charge, and require no external devices to operate. However, this lifetime is still quite short.

It is our hope that by developing a high efficiency, targeted wavelength LED the need for intensive processing can be reduced, in turn allowing for devices which can be used for long periods of time and in remote locations.

It has been shown that wavelengths of 850nm are particularly useful for these applications, because the contrast between light intensity in blood vessels and surrounding tissues is maximized [4]. As such, we have chosen to target this 850nm peak for our design.

II. PHYSICS AND TECHNOLOGY

The device we propose is an AlGaAs/InGaAs lateral MQW structure. Documentation of the design process will be divided into the following topics: introductory TCAD basis, a study of the effect of well width and indium content on output in an idealized vertical single quantum well system, the effect of changing from a single quantum well structure to a MQW structure, and finally changes in the system output when going from the idealized vertical structure to a lateral structure.

II.1 TCAD BASICS AND ADDITIONAL BACKGROUND

Design of modern devices is contingent on the use of Technology Computer-Aided Design (TCAD) software. TCAD software is typically reliant on a form of finite element analysis (FEA). Due to the increasing cost and time commitment required to fabricate a new device, and the myriad issues that can arise during processing, confirming device behavior before attempting to fabricate it is paramount to a successful device.

When modeling the electrical behavior of a semiconductor device, there are three equations which must be used. They are Poisson's equation (1), the continuity equations (2), and the current density equations (3) [6]. The equations as formulated for electrons are presented here, with analogous equations defined for hole behavior.

$$\nabla^2 V = -\frac{\rho}{\epsilon_r \epsilon_s} \quad (1)$$

$$\frac{\partial n}{\partial t} = \frac{1}{q} \vec{\nabla} \cdot \vec{J}_n + G_n - R_n \quad (2)$$

$$\vec{J}_n = q\mu_n n \vec{E} + qD_n \vec{\nabla} n \quad (3)$$

The equations given by (1) and (2) are partial differential equations. In order to accurately represent the device behavior, they must be solved numerically. This is done via construction of

a mesh, where the device to be simulated is broken up into many points and solved using boundary conditions generated by the neighboring points, device edges, and contacts. Specific additional physical models may be used as well.

II.2 WAVELENGTH TUNING

The first iteration of the device is a single quantum well structure using a vertical design for exploration of the effects of the quantum well structures on the device output. A cartoon of this can be seen in Figure 2. The decision was made to use a bulk of $\text{Al}_{0.6}\text{Ga}_{0.4}\text{As}$. This decision was due to the ability to lattice match to a Ge substrate in the final lateral design, as will be detailed further in Section II.4.

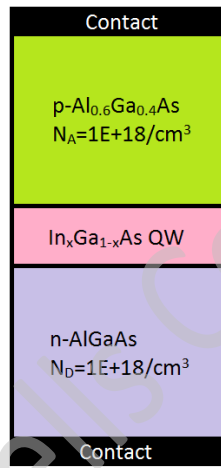


Figure 2: Vertical Design Schematic

The contacts were made to be ohmic, and a value of $N_A=10^{16} \text{ cm}^{-3}$ and $N_D=10^{16} \text{ cm}^{-3}$ were selected for the initial explorations. For the first study, the well width was varied between 3nm to 15nm in 2nm increments, and the indium mole fraction was allowed to vary from 0% to 12% in 2% increments at each well width. For each simulation run, the emission spectrum was plotted as the total internal spontaneous emission rate by wavelength. This data was exported for further analysis using MATLAB.

With the data from the simulations loaded in to MATLAB, the quantities of interest were the peak emission wavelength and the FWHM of the emission spectrum. In Figure 3, the emission spectrum for various indium contents and a 7nm quantum well width is presented. We can clearly see the expected redshift for increasing indium content as the band gap is reduced. Additionally, we can see a decrease in the secondary peak corresponding to secondary quantum energy levels as we increase the indium content.

In the quantum well, the energy levels corresponding to the emission energies can be modeled as a finite potential well, and found by solving the Schrödinger equation for its energy eigenvalues. The general form of these solutions in the case of the infinite square well is given

by (4). This clearly shows the inverse dependence on both the mass of the particle m and the well width, a . The finite square well has energy levels slightly below this, for which a closed form solution does not exist. These levels must be found numerically instead. However, for present purposes only the qualitative description of the energy levels decreasing as the well width depth decreases is of importance in the finite well analysis. As such, the peak emission wavelength should increase significantly with increased well width, and the effect of narrowing the band gap with additional indium content should be complemented by the increased energy levels.

$$E_n = \frac{(\pi\hbar n)^2}{2ma^2} \quad (4)$$

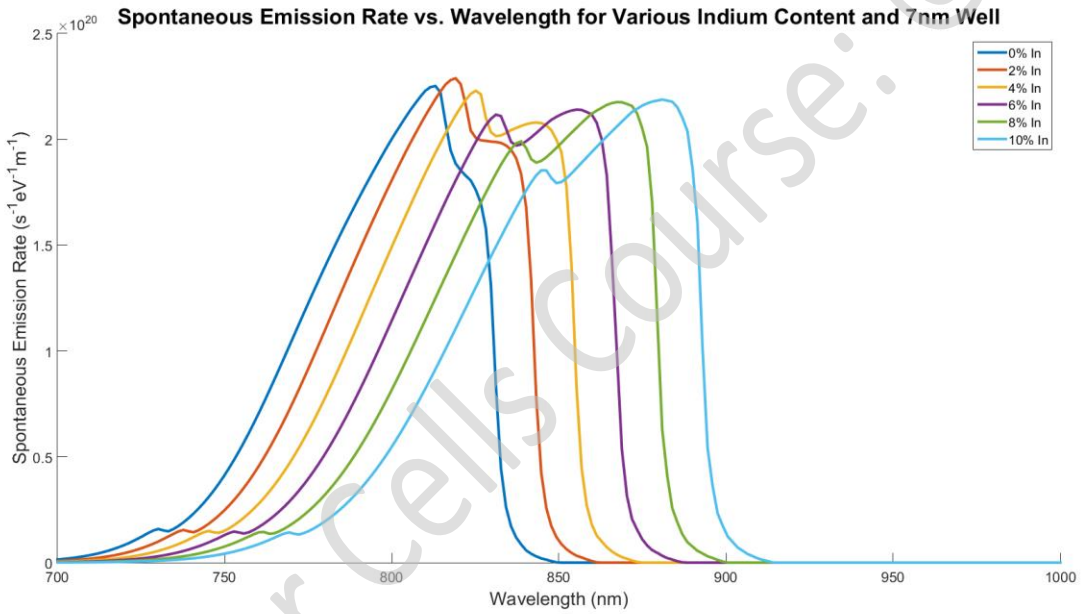


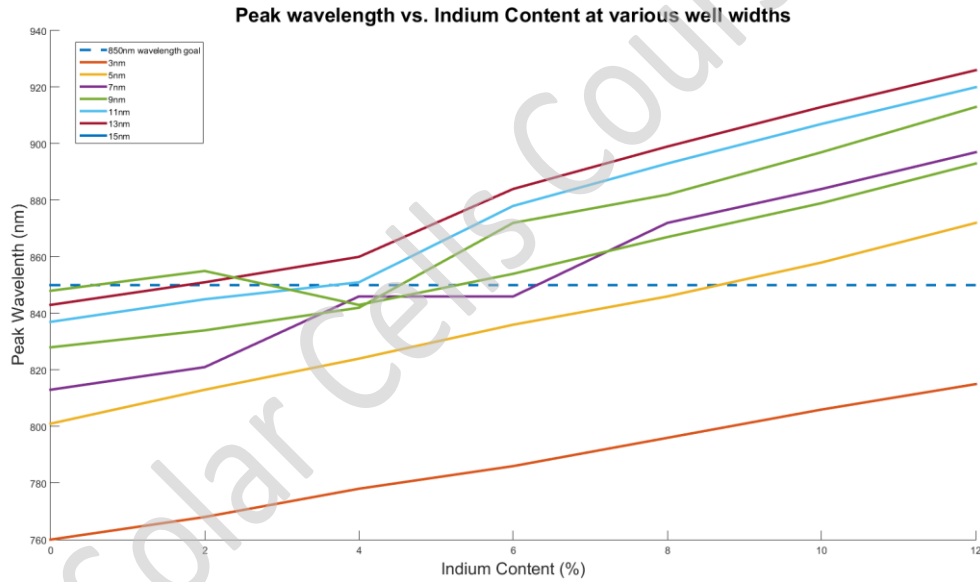
Figure 3: Emission Spectrum for Varied Indium Content at 7nm Well

In support of the provided qualitative description, the following procedure was performed: the structure as given in Figure 2 was simulated for the indium content and well width ranges as indicated, and the peak wavelength was extracted and plotted using MATLAB. Following this, the full width at half max (FWHM) was extracted using the indium content giving an emission nearest to 850nm for each well width and plotted in an effort to select the well width and indium content corresponding to the most focused 850nm output. These contents have been gathered in to Table 1. It is worth noting that we chose to not allow the indium content exceed 12%, due to the increasing lattice mismatch and decreasing critical thickness for strained quantum well structures. Finally, the results of the study of the effect of well width and indium content on peak emission wavelength have been gathered in to Figure 4.

Table 1: Indium Contents for producing near 850nm

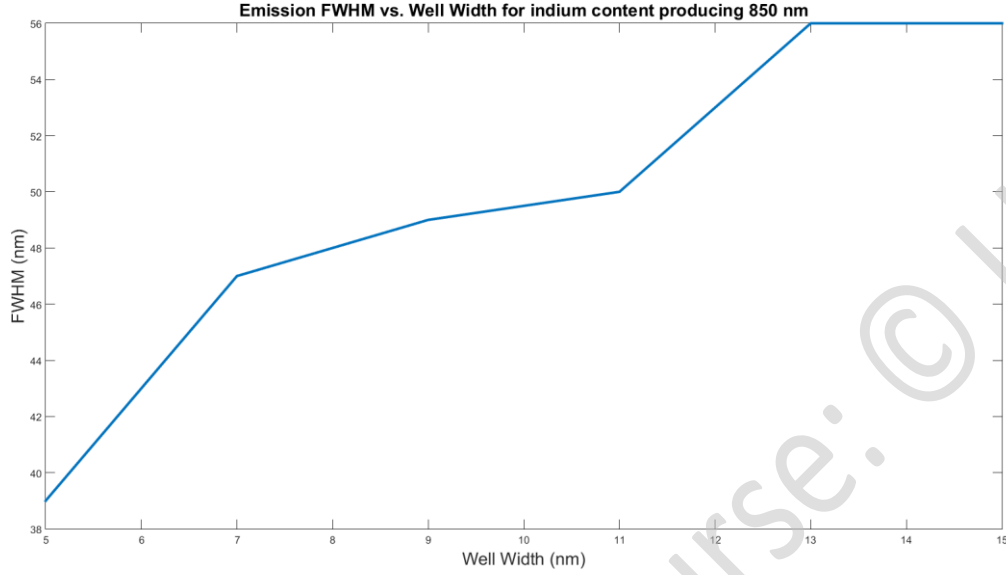
Well Width	Indium Content	Wavelength
3nm	N/A	N/A
5nm	9%	852 nm
7nm	6%	846 nm
9nm	5%	866 nm
11nm	4%	851 nm
13nm	2%	851 nm
15nm	6%	854 nm

The solutions to the Schrödinger equation inside the wells was solved additionally, so as to create a well with only one allowed energy level along the direction of confinement. This was done in order to minimize the spread in emitted wavelengths and hit the targeted wavelength as precisely as possible. Crosslight allows for self-consistent solutions to the time-independent Schrödinger equation (5), with the relevant boundary conditions given for heterojunctions (6).

Figure 4

In addition to plotting the FWHM, the time-independent Schrödinger equation given by (5) was solved for the quantum well. The conduction band edge was taken to be a potential of 0, while the well depth, given by $-\Delta E_c$ with $\Delta E_c > 0$ was calculated from the electron affinities and band gaps as given by Vegard's law. The well was taken as extending from $-a$ to a , with $a=2.5\text{nm}$. Additionally, due to the differences in m^* in the AlGaAs and InGaAs regions, the relevant boundary conditions for continuity of the derivative of the wave function were updated to those given by (6).

Figure 5



$$\left[\frac{-\hbar^2}{2m^*} \frac{\partial^2}{\partial x^2} - \Delta E_c \right] \psi(x) = E\psi(x) \quad (5)$$

$$\frac{1}{m^*(x^-)} \frac{\partial \psi}{\partial x} = \frac{1}{m^*(x^+)} \frac{\partial \psi}{\partial x} \quad (6)$$

$$P_{A_x B_{1-x}} = x \cdot P_A + (1 - x) \cdot P_B \quad (7)$$

The method for solving the finite well problem mirrored that outlined by Griffiths [7], with κ and μ as given by (8) and (9), with κ defined for the AlGaAs regions and μ defined inside the well. Using Vegard's Law (7), and affinity of AlAs, InAs, and GaAs as given by Table 2, we calculated a well depth of 0.4167 eV. From here, the solutions to Schrödinger's equation in the 3 regions can be simplified by assuming an odd symmetry to the well. We can therefore express ψ using (10).

$$\kappa = \frac{\sqrt{-2m^*E}}{\hbar} \quad (8)$$

$$\mu = \frac{\sqrt{2m^*(E + \Delta E_c)}}{\hbar} \quad (9)$$

$$\psi(x) = \begin{cases} Be^{\kappa x}, & x < -a \\ C\cos(\mu x), & -a < x < a \\ -Be^{-\kappa x}, & x > a \end{cases} \quad (10)$$

Applying the boundary conditions in (6), we can express the solutions for E in terms of κ and μ using the transcendental equation (11). The solutions to this equation indicate the number of bound states, and can be seen in Figure 6. We clearly have only a single bound state, as desired to give the narrowed emission spectrum possible. The extracted value for E_1 was found to be -0.0718 eV. From here, ψ was plotted superposed over the potential, as well as the energy levels as seen in Figures 7 and 8 respectively.

$$-\frac{m_{AlGaAs}^*}{m_{InGaAs}^*} \tan(\mu x) = \frac{\mu}{\kappa} \quad (11)$$

Table 2: Material Parameters used to solve TISE in MATLAB

Parameter	Value	Ref (if applicable)
AlAs electron affinity	3.50 V	
GaAs electron affinity	4.07 V	
InAs electron affinity	4.9 V	
Aluminum content	60%	
Indium content	9%	

Figure 6

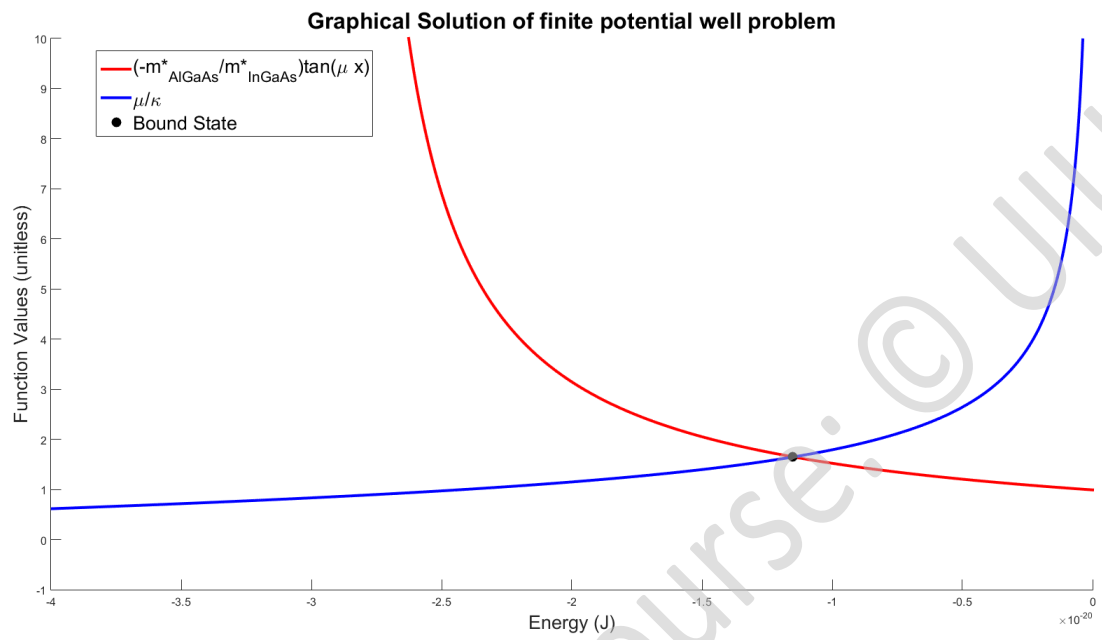


Figure 7

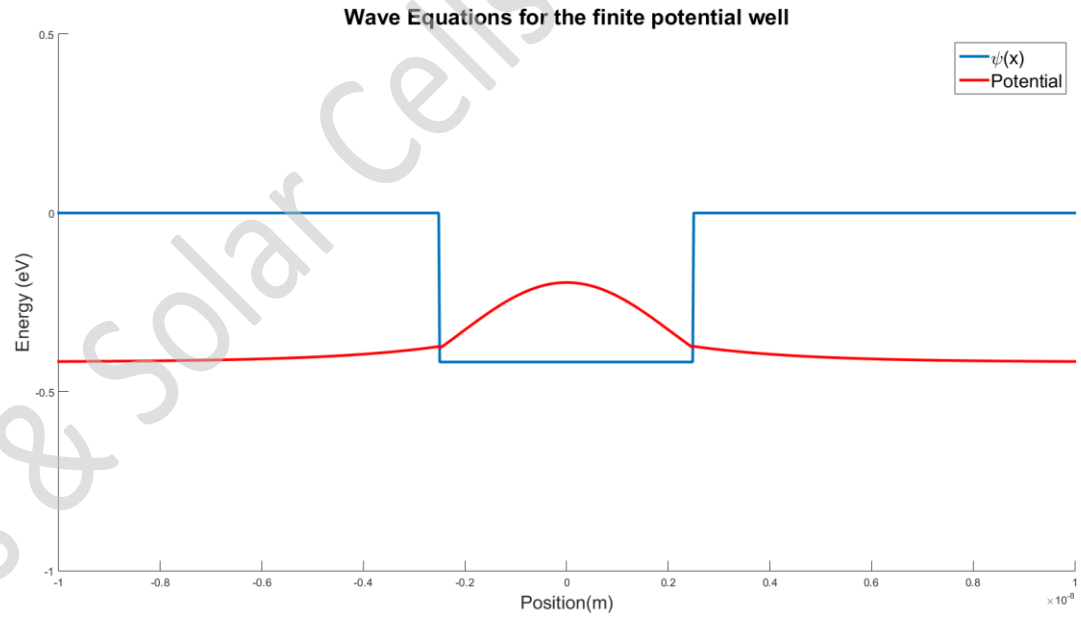
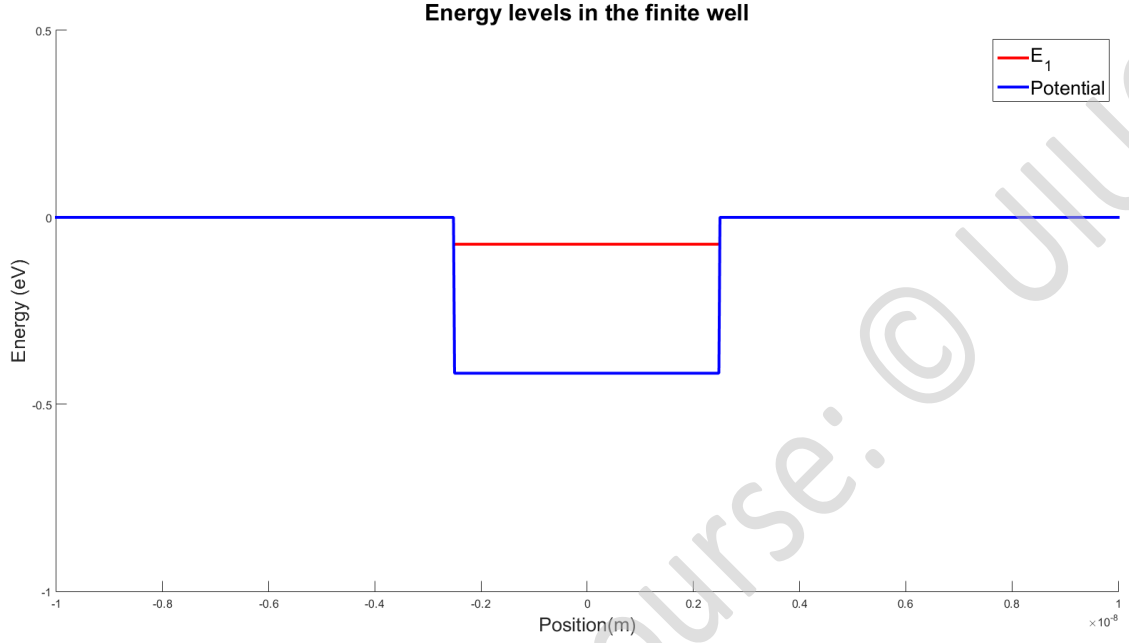


Figure 8



II.3 SINGLE QUANTUM WELL TO MQW STRUCTURE

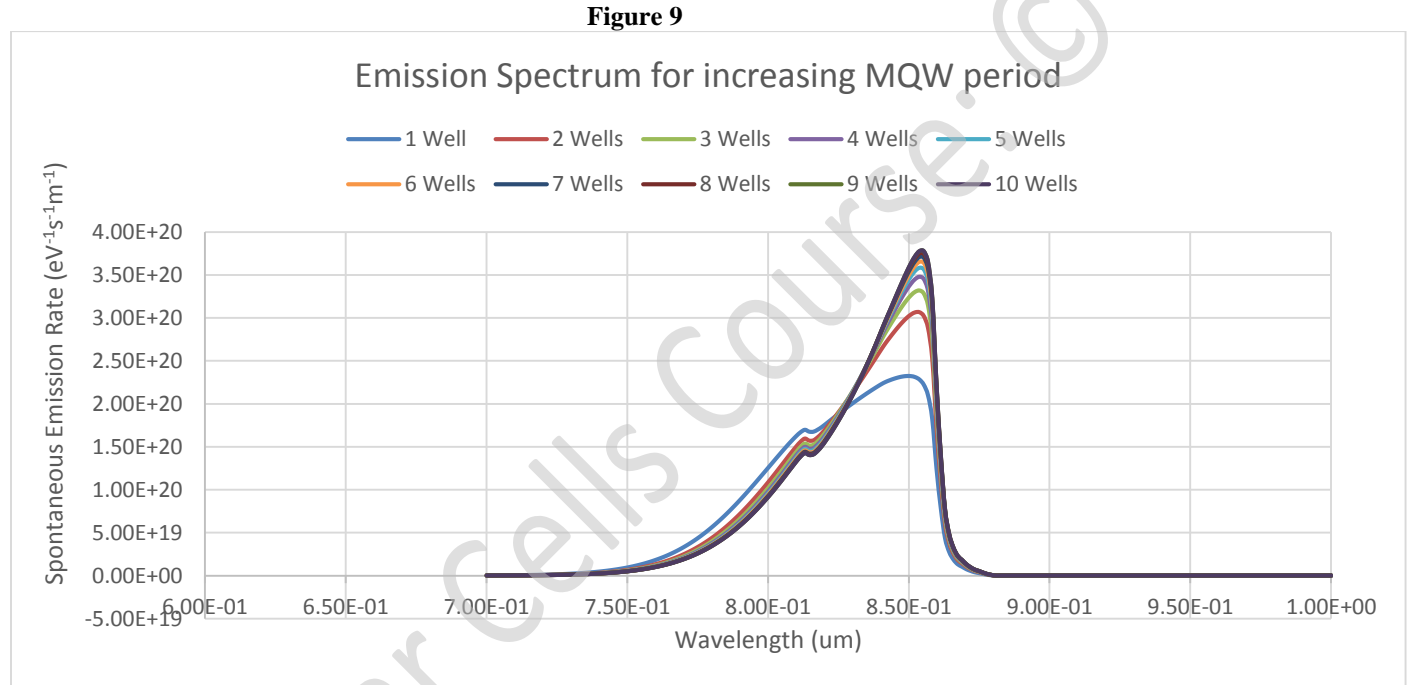
For this study, the device was altered to include an MQW structure, or multiple quantum wells. The new structure mirrors that of Figure 2, but with the single quantum well replaced with a multiple quantum well structure. The purpose of this study was to examine the effect of the MQW. Specifically, the impact on efficiency and the total emission rate were of concern. We expect as the number of wells increases, the number of photons emitted should increase due to the increased number of confinements.

Before optimizing the number of quantum wells, the well spacing must be taken under consideration. Studies have shown that for the $\text{In}_{0.2}\text{Ga}_{0.8}\text{As}/\text{GaAs}$ system, the critical thickness t_c is given as 24 bi-layers, or 69.6936 Å [8]. Additionally, for a quantum well of $0.5t_c$ the critical thickness, the barrier layer may be $0.4t_c$ for up to 10 periods [8]. For our present system, we have an $\text{In}_{0.09}\text{Ga}_{0.92}\text{As} / \text{Al}_{0.6}\text{Ga}_{0.4}\text{As}$ quantum well structure. The bulk $\text{Al}_{0.6}\text{Ga}_{0.4}\text{As}$ is lattice matched to Ge, with $a = 5.658$ Å [9]. Compared to the lattice constant of GaAs, $a = 5.65325$ Å, this gives a mismatch of 0.084%. Additionally, the lattice constant varies linearly with mole fraction, and so for our purposes we will assume that the critical thickness varies approximately linearly as well. This assumption is valid in accordance with the Matthews-Blakeslee model, as t_c is inversely proportional to the lattice mismatch, f , while the logarithm of t_c/b will vary more slowly [10]. This means that our assumed 5nm quantum well width is approximately $0.5t_c$, and so we may use narrow barriers for up to 10 periods.

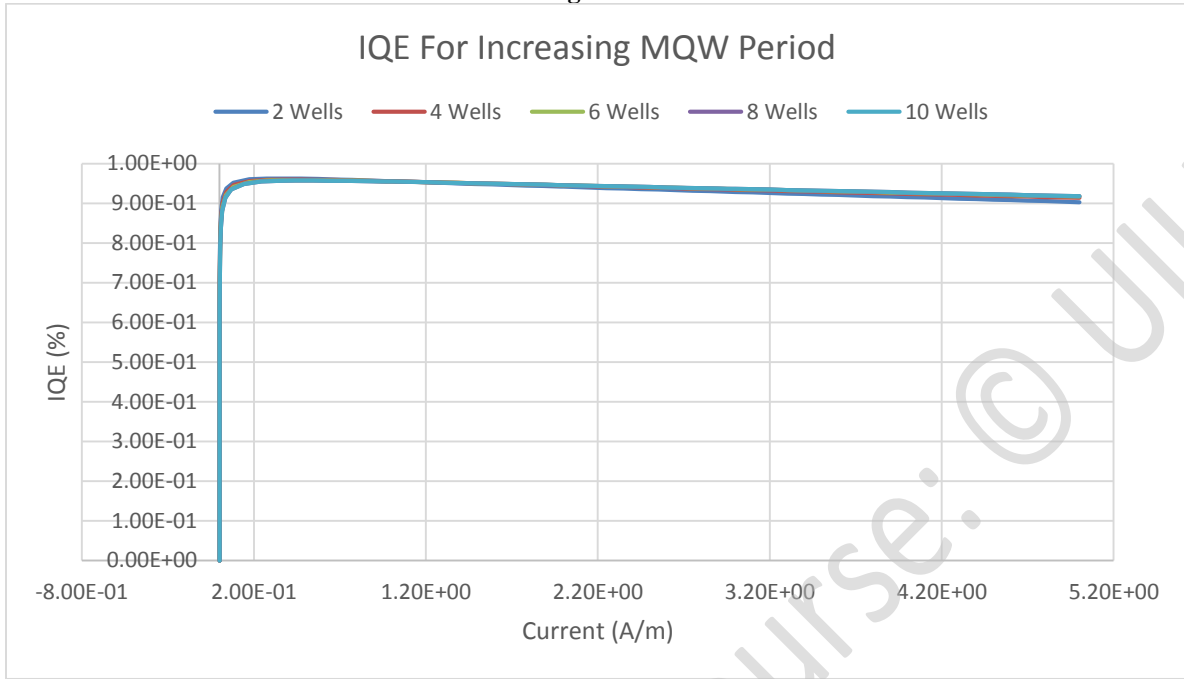
$$t_c = \frac{b}{2\pi f} \frac{1 - v \cos^2 \alpha}{(1 + v) \cos \lambda} \left(\ln \frac{t_c}{b} + 1 \right) \quad (12)$$

Simulations have been run using a 5nm well with a 5nm barrier, and the main quantity of interest is the peak emission rate, giving the total number of photons generated per eV per second per meter. The barrier width of 5nm has the additional benefit of being long enough that the wave function for each well has decayed significantly enough to have minimal interference with each other, as can be seen in the solution to the finite well problem detailed in Section II.2.

The results of this study are gathered in Figure 9. As anticipated, the peak emission rate increases proportionally to the number of periods, confirming the increase in output power with the MQW period. Our device is meant to be a high efficiency, high output device and so the MQW period should be maximized. However, based on the assumptions in obtaining these values of t_c varying linearly is indium content, we propose a maximum number of 6 periods.



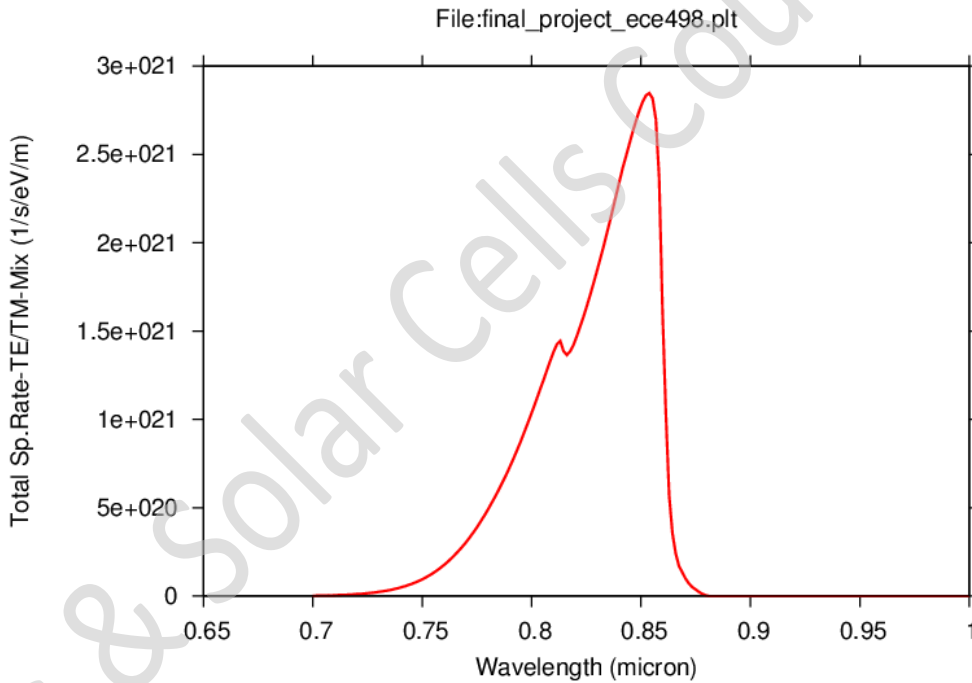
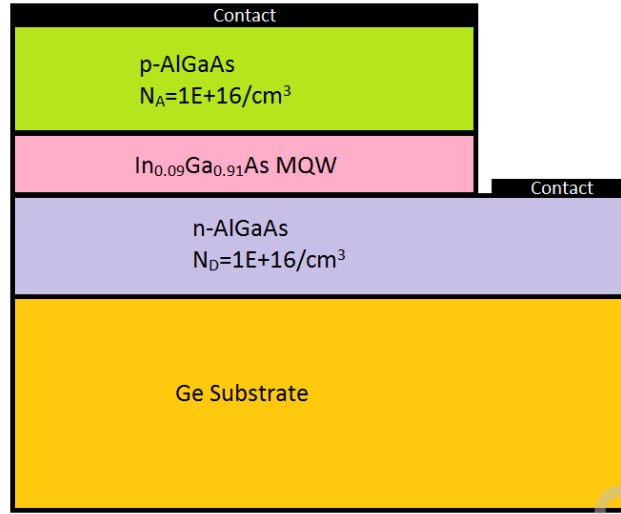
Additionally, the impact of the MQW period on the IQE was documented for the case of 2, 4, 6, 8, and 10 quantum wells. This data has been gathered in to Figure 10. We can see that the period has no discernable impact on the efficiency for the basic set of simulation parameters.

Figure 10

II.4 LATERAL DESIGN

After optimizing the QW thickness, spacing, and period, we moved towards a device for fabrication. We propose a lattice matched Ge substrate, due to the ability to selectively etch Ge using XeF_2 dry etches, with the ability to etch as fast as 6mm/hr [11]. A depiction of the structure for the lateral design can be seen in Figure 11. Additionally, the doping has been updated to achieve a peak electron concentration of $\sim 0.5\text{E}+17/\text{cm}^3$ in the MQW confinements at the on-voltage to maximize the impact on the luminous efficiency [12]. This design was chosen in order to make a device which can be fabricated. The vertical design is efficient for optimizing the active regions of the device, but the lateral design reflects the geometry of modern devices. However, this offers unique challenges such as current crowding [12]. In our present design, this was addressed minimally by making the p-layer contact as large as possible and doping the layer immediately below the contacts very heavily, with $N_A=N_D=1\text{E}+20/\text{cm}^3$.

Figure 11: Lateral Device Design



II.5 FINAL RESULTS

The final design of the device has been summarized in Table 3. The bulk aluminum is given as 60% to lattice match Ge and minimize defects prior to lift-off. The indium content of 9% has been selected to target the selected wavelength when taken in consideration with the quantum well levels. The doping in the P regions was selected to be $1 \times 10^{18} \text{ cm}^{-3}$, and the N regions were doped at $1 \times 10^{16} \text{ cm}^{-3}$. The quantum wells and separation between wells are set to 5nm. This achieves a peak emission wavelength of 854 nm.

Table 3: Final Design Parameters

Parameter	Value
Aluminum Content (Bulk)	60%
Indium Content (QW)	9%
MQW Period	6
Peak Wavelength	854 nm
P doping	1E+18/cm ³
N doping	1E+16/cm ³
Quantum Well Width	5 nm

The band diagram for the final device is shown in Figure 12. We can clearly see the MQW structure at approximately 0.5um from the edge of the image. In order to confirm the concentration of carriers in the MQW, the electron concentration as a function of position was plotted and shown in Figure 13. As desired, the electrons are confined to the well aiding in radiative recombination.

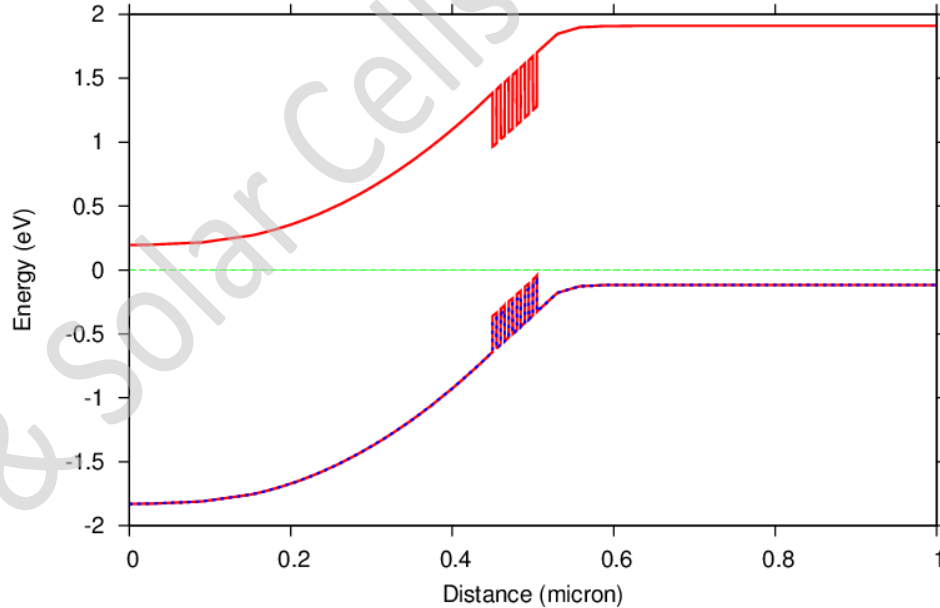
Figure 12: Band Diagram for Final Design

Figure 13: Electron Concentration as a function of Position

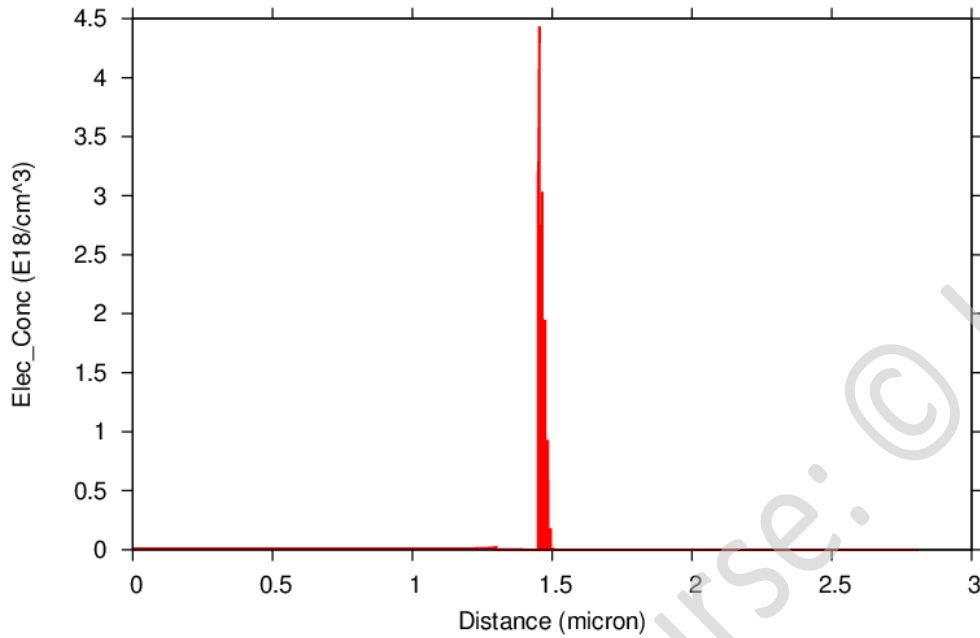
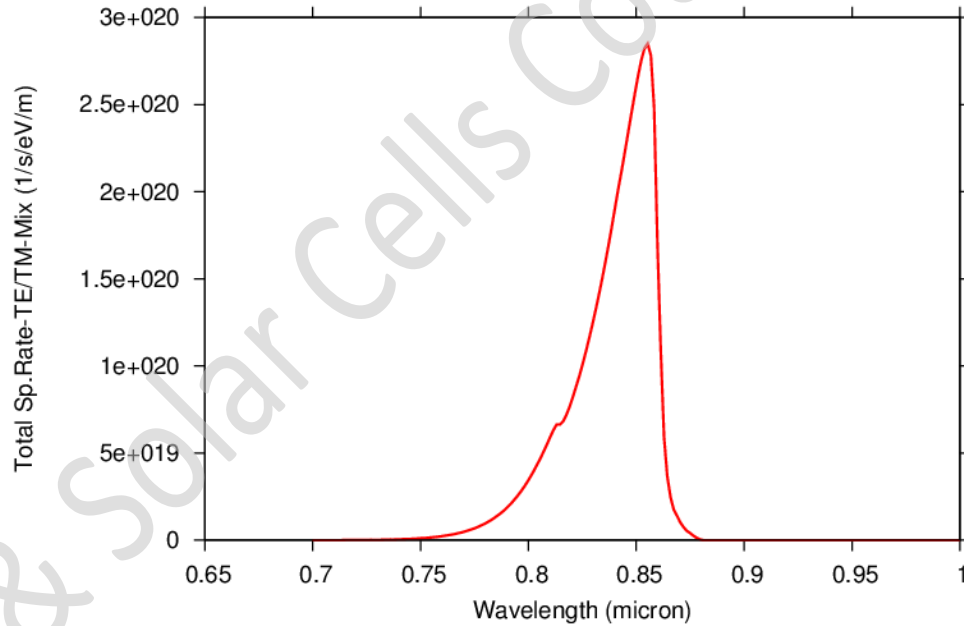
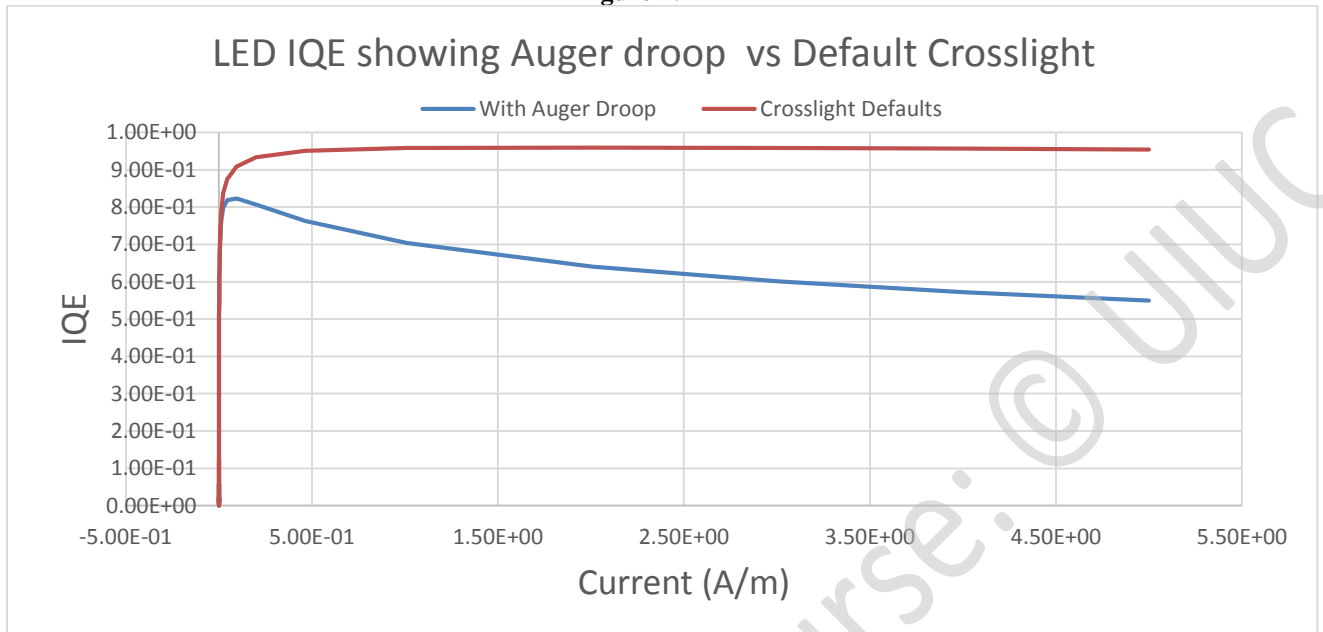


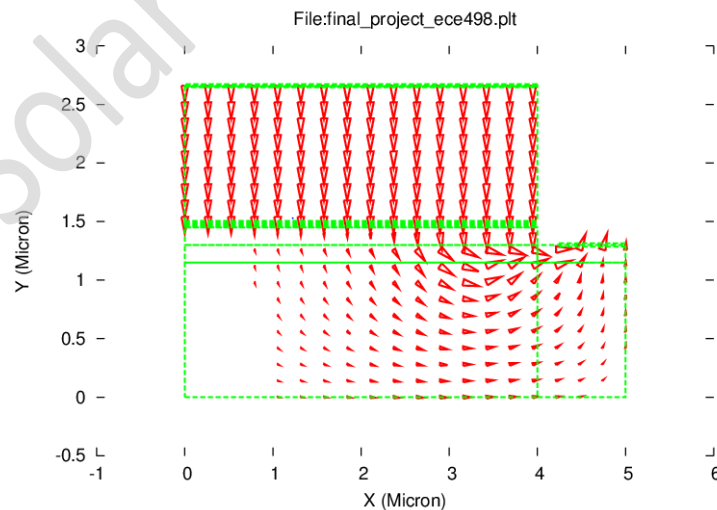
Figure 14: Emission Spectrum for Final Design



The total spontaneous emission rate as a function of wavelength is given in Figure 14. The desired peak at approximately 854 nm can be seen, as well as the very narrow targeted emission spectrum. There is a slight secondary peak around 800 nm, but this is sufficiently small compared to the main peak so as to not have a noticeable impact on performance.

Figure 15

In Figure 15, the internal quantum efficiency can be seen as a function of current. This plot also highlights one of the major limitations of simulation software. The default Crosslight simulation equations do not accurately account for droop, the well-documented phenomenon in which efficiency in LEDs drops as current increases [13]. It has been shown that Auger recombination is a major contributor to droop, particularly due to the high carrier concentrations in MQW structures [13]. As such, the values for the Auger recombination coefficients were manually updated to reflect those found experimentally for 5nm InGaAs quantum well structures [14]. The values used were $0.65\text{E-}28\text{cm}^6/\text{s}$ for both electron and hole lifetimes [14]. The effect of this and the more realistic IQE can be seen plotted together in Figure 15.

Figure 16: Current Vectors in the Lateral Design

In an effort to investigate current crowding effects, the current was plotted as a vector on the 2D device structure. We can see a strong current near the mesa edge, indicating current crowding. However, the spacing and doping near the contacts keep current uniform in the p-AlGaAs layer,

which the n contact is allowed to draw current from large regions of the device albeit at lower magnitudes. It is recommended in future studies to explore this phenomena and implement solutions before fabricating a device like the one presented here.

III. SUMMARY

We have proposed a lateral MQW based AlGaAs/InGaAs LED lattice matched to Ge to emit at 854 nm for use in NIR medical applications. The device presented has been optimized to achieve a targeted wavelength and high output power. The goal is to ultimately create a device which can be used to reduce power demands in existing vein viewing technology by reducing the need for computer post processing.

The design of such a device relies on a strong knowledge of quantum and semiconductor physics. However, the use of commercially available TCAD software can aid immensely in ensure the device operates as desired before taking on the costs associated with fabrication. The inherent risk with this approach is in inaccurate simulations. As was shown in Section II.5, a designer must have a strong understanding of what the results for a device should be, and a firm grasp of the TCAD software itself to optimize its behavior for the specific designs. If this is not done, the results can be wildly inaccurate and not capture performance of devices shown experimentally. Ideally, the simulations and experimental findings should be as much in agreement as possible.

Some of the major topics to be addressed with before fabricating our proposed device are packaging and the use of encapsulants to extract as much of the generated light as possible, as well as direct it efficiently to keep it focused on the skin of a patient. Current crowding must also be addressed to keep device lifetimes as high as possible. In medical applications, the reliability of the device is of major concern due to the significant risks should devices fail prematurely.

Some additional topics to be addressed are the precise metal to be used for contacts. We have presented a design using heavily doped layers in the semiconductor immediately below the contacts to aid in ensuring ohmic contacts are made, but the metal must still be selected. Additionally, due to the lifted off design, the device is able emit light from the bottom and as such Bragg reflectors or reflective contacts can be used to increase light extraction from the active region of the device.

IV. REFERENCES

- [1] Paquit, V.C., Tobin, K.W., Price, J.R., Meriaudeau, F., “3D and Multispectral Imaging for Subcutaneous Veins Detection.” [Optics Express, Vol. 17, Issue 14. Pp.11360-11365 \(2009\).](#)
- [2] B.L. Horecker, “The Absorption Spectra of Hemoglobin and its Derivatives in the Visible and Near Infra-Red Regions,” [J. Biol. Chem. 1943 148: 173.](#)
- [3] S. Ganesh, *Depth and Size Limits for the Visibility of Veins Using the VeinViewer Imaging System*. Masters Thesis. [University of Tennessee and University of Memphis.](#) 2007.
- [4] N.J. Cuper, J.H. Klaessens, J.E. Jaspers, R. de Roode, H.J. Noordmans, J.C. de Graaff, R.M. Verdaasdonk, “The use of near-infrared light for safe and effective visualization of subsurface

blood vessels to facilitate blood withdrawal in children.” [Medical Engineering & Physics, Volume 35, Issue 4, April 2013, Pages 433-440](#)

[5] Christie Medical. [Our Technology](#). Website. Accessed Apr. 25 2016.

[6] Leburton, J.P., Basic Equations for Semiconductor Devices, [ECE 441 class notes, UIUC](#). Included in Materials folder with submission.

[7] Griffiths, David J. Introduction to Quantum Mechanics, 2nd edition, Pearson Prentice Hall, 2004.

[8] M. Madebo, B.F. Usher, J. Riley, [28th Annual Condensed Matter and Materials Meeting, Feb. 2004](#).

[9] Semiconductors on NSM. [ioffe.ru](#)

[10] J.W. Matthews, A. E. Blakeslee, “Defects in Epitaxial Multilayers I. Misfit Dislocations.” [Journal of Crystal Growth 27 \(1974\) 118-125](#).

[11] Y. Bai, E.A. Fitzgerald, “Ge/III-V Heterostructure and their Applications in Fabricating Engineered Substrates,” [Electrochemical Society Transactions. 2010 volume 33, issue 6, 927-932](#)

[12] Schubert, E.F., [Light-Emitting Diodes](#). 2nd ed, Cambridge University Press, 2007.

[13] J. Iveland, L. Martinelli, J. Peretti, J. S. Speck, C. Weisbuch, “Direct Measurement of Auger Electrons Emitted from a Semiconductor Light-Emitting Diode under Electrical Injection: Identification of the Dominant Mechanism for Efficiency Droop,” [Physical Review Letters 110, 177406 \(2013\)](#).

[14] S. Hausser, A. Fuchs, A. Hangleitner, K. Streubel, W.T. Tsang, “Auger recombination in bulk and quantum well InGaAs,” [Applied Physics Letters 56, 913 \(1990\)](#)